Insights into Spontaneous Solid Electrolyte Interphase Formation at Magnesium Metal Anode Surface from Ab Initio Molecular Dynamics Simulations

Journal:	*ACS Applied Materials & Interfaces*
Manuscript ID	am-2021-07864g.R2
Manuscript Type:	Article
Date Submitted by the Author:	n/a
Complete List of Authors:	Agarwal, Garvit; Argonne National Laboratory Materials Science Division Howard, Jason David; Argonne National Laboratory, MSD Prabhakaran, Venkateshkumar; Pacific Northwest National Laboratory, Physical Sciences Division Johnson, Grant; Pacific Northwest National Laboratory, Chemical Physics and Analysis Murugesan, Vijayakumar; Pacific Northwest National Laboratory, Energy & Environmental Division Mueller, Karl; Pacific Northwest National Laboratory, Physical and Computational Sciences Directorate Curtiss, Larry; Argonne National Laboratory, Materials Science Assary, Rajeev; Argonne National Laboratory, Materials Science Division

Insights into Spontaneous Solid Electrolyte Interphase Formation at Magnesium Metal Anode Surface from *Ab Initio* Molecular Dynamics Simulations

Garvit Agarwal[a,b,*], Jason D. Howard[a,b], Venkateshkumar Prabhakaran[b,c], Grant E. Johnson[b,c], Vijayakumar Murugesan[b,c], Karl T. Mueller[b,c], Larry A. Curtiss,[a,b] and Rajeev S. Assary[a,b,*]

[a] Materials Science Division, Argonne National Laboratory, Lemont, IL, 60439, USA
[b] Joint Center for Energy Storage Research (JCESR), Argonne National Laboratory, Lemont, IL, 60439, USA
[c] Pacific Northwest National Laboratory, Richland, WA, 99352, USA

Corresponding authors(*): GA: garvit.iitr@gmail.com, RSA: assary@anl.gov
Phone: 630-252-3536

Abstract

Spontaneous chemical reactivity at multivalent (Mg, Ca, Zn, Al) electrode surfaces is critical to solid electrolyte interphase (SEI) formation, and hence, directly affects the *longevity* of batteries. Here, we report an investigation of the reactivity of 0.5 M $Mg(TFSI)_2$ in 1,2-dimethoxyethane (DME) solvent at a Mg(0001) surface using *ab initio* molecular dynamics (AIMD) simulations and detailed Bader charge analysis. Based on the simulations, the initial degradation reactions of the electrolyte strongly depend on the structure of the $Mg(TFSI)_2$ species near the anode surface. At the surface, the dissociation of $Mg(TFSI)_2$ species occurs *via* cleavage of the N-S bond for the solvent separated ion pair (SSIP) and *via* cleavage of the C-S bond for the contact ion pair (CIP) configuration. In the case of the CIP, both TFSI anions undergo spontaneous bond dissociation reactions to form atomic O, C, S, F, and N species adsorbed on the surface of the Mg anode. These products indicate that the initial SEI layer formed on the surface of the pristine Mg anode consists of a complex mixture of multiple components such as oxides, carbides, sulfides, fluorides, and nitrides. We believe that the atomic level insights gained from these simulations will lay the groundwork for the rational design of tailored and functional interphases that are critical for the success of multivalent battery technology.

Keywords: Mg-Battery, Solid-Electrode Interface, Density functional theory, Ab initio Molecular Dynamics, Interfacial reactivity, Reaction mechanisms

Introduction

The widespread adoption of clean energy, such as solar and wind, and the electrification of the transportation sector requires development of next generation energy storage technologies that are safer, cheaper, and possess higher energy density compared to state-of-the-art Li ion batteries[1,2,3,4]. Multivalent batteries, especially those using divalent metallic Mg, Ca, and Zn as anode materials, are promising alternatives to conventional Li ion batteries due to their abundance, better chemical stability, and higher theoretical specific capacity[5,6,7]. However, there are several fundamental challenges associated with the development of next-generation multivalent batteries. Lack of compatible electrolytes with the metallic anodes, stable electrode-electrolyte interphases, reversible plating, and stripping of divalent cations are some of the crucial challenges[7,8]. The decomposition of salt and solvent molecules in the electrolyte at the anode surface can form a multi-layered passivating film known as the solid electrolyte interphase (SEI), consisting of various organic and inorganic components[9,10]. In the case of Li-ion batteries, the SEI film is ionically conducting and electronically insulating. Thus, it allows the diffusion of Li ions through the electrode-electrolyte interphase and prevents continuous degradation of electrolyte at the anode surface. As mentioned earlier, in multivalent batteries the design of stable and functional SEI layers is still an outstanding challenge[11,12,13], where a fundamental understanding of the *structure and composition* of the SEI layer is essential, but currently lacking.

Experimental studies have focused on identifying suitable solvent and salt combinations that allow reversible electrodeposition of multivalent metal ions. For example, Ca containing salts, such as $Ca(ClO_4)_2$ and $Ca(BH_4)_2$, in tetrahydrofuran (THF) solvent have shown reversible plating and stripping of Ca[14,15]. Similarly, in the case of Mg batteries, electrolytes containing ether-based solvents (e.g., tetrahydrofuran (THF) and glymes) have been successfully used for reversible plating and stripping of Mg[16,11]. Several experimental studies have reported improved plating and stripping performance of Mg containing electrolytes in the presence of chloride (Cl^-) ions[17,18,19,20]. The improved performance in the presence of Cl^- ions is attributed to the presence of surface adsorbed anionic (Cl^-) species resulting in better stability of the salt at the Mg anode. Connell *et al.*[21] reported the cooperative effect of multiple anions in improving the reversibility of non-aqueous electrolytes in the mixed-anion systems. The authors reported anion association strength as the common descriptor for improved reversibility of divalent metal salts in non-aqueous solvents. The structure and conformational variations of the bis(trifluoromethanesulfonyl)imide (TFSI) anion of the $Mg(TFSI)_2$DME (DME: dimethoxy ethane) adduct have been investigated using a combination of solid state nuclear magnetic resonance (NMR) spectroscopy and quantum mechanical calculations[22]. The *cis* and *trans* conformers of the TFSI anion have been identified and the *cis-trans* conversion rates at different temperatures have been computed. Hahn *et al.*[23] reported the important role of the interplay between the cation-anion and cation-solvent coordination strengths on the Ca electrodeposition. These investigations show that progress has been made in the development of suitable electrolytes and the understanding of their electrochemical responses for multivalent batteries. However, improvements in the interfacial stability, ionic conductivity, and cycle lifetime of these electrolytes are needed for their application in commercial multivalent batteries. The design of a stable and functional SEI layer in multivalent batteries requires a detailed molecular level

understanding of the complex electrochemical reactions of the salt and solvent species of the electrolyte with the anode surface.

Theoretical methods, such as density functional theory (DFT) and classical molecular dynamics (MD) simulations, have provided crucial insights into the bulk structure of the liquid electrolytes and their atomic-level interactions with the anode surface[24,25,26,27,28,29]. Selected investigations are discussed here. *Ab initio* molecular dynamics (AIMD) simulations have been performed to understand the decomposition reaction mechanisms and surface reactivity of commonly used Li salts (LiTFSI, LiFSI) with the Li metal surface for applications in Li-S batteries[30-33]. These AIMD simulations have provided novel insights into the role of charge transfer from the Li metal surfaces in the reactivity and decomposition mechanisms of the electrolytes. The LiFSI salt was found to undergo extensive decomposition forming LiF as the major SEI product. In comparison, the reduction reaction of the LiTFSI salt results in formation of larger fragments as the initial SEI components[30]. The AIMD simulations have also shown higher reactivity of charged Li metal surfaces toward electrolyte decomposition. The salt and solvent molecules of the various electrolytes were found to decompose to a greater extent under electron-rich conditions[32,33]. The effect of surface passivation layers, such as Li_2O, LiOH, and Li_2CO_3 on the reactivity of the LiTFSI salt in DME solvent has been investigated using a combination of AIMD simulations and X-ray photoelectron spectroscopy (XPS) measurements[34]. These predictive simulations allow for identification of key SEI products formed during early stages of electrolyte decomposition at the surface of the anode. Recently, Young *et al.*[35] performed AIMD simulations to investigate the decomposition reaction mechanism of ethylene carbonate (EC) (a commonly used solvent in Li ion batteries) on the Ca (001) surface. The authors reported two distinct mechanisms of EC decomposition resulting in the formation of carbon monoxide (CO) and carbonates. They also investigated the effect of the presence of $Ca(ClO_4)_2$ salt on the decomposition mechanism of EC molecules and proposed key SEI products, such as CaO, $Ca(OH)_2$, and $CaCO_3$ formed on the surface of the Ca metal anode. Similarly, AIMD simulations of EC-based electrolytes containing $LiPF_6$, $Ca(PF_6)_2$, and $AlCl_3$ as the salt have been performed to understand the reactivity of the electrolytes with Li, Ca, and Al metal anodes, respectively[36]. The AIMD simulations showed faster decomposition of EC solvent molecules on Li and Ca anodes, which was attributed to faster charge transfer rates from Li and Ca surfaces as compared to a reference Al (001) surface. Das *et al.,* performed simulations that compare the reactivity and stability of ethyl methyl carbonate (EMC) and EC solvent molecules with pure Al and lithiated Al anode surfaces[37]. The higher stability of EMC compared to EC is attributed to less charge transfer from the Al and LiAl surfaces, respectively. Lowe *et al.*[38] carried out nudged elastic band (NEB) calculations to compute the energy barriers and identify reaction pathways for decomposition of dimethoxy ethane (DME) solvent molecules on Mg (0001), MgO (100), and $MgCl_2$ (0001) surfaces. Based on this investigation, the higher energy barriers for decomposition of DME on MgO (100) and $MgCl_2$ (0001) surfaces indicate the relatively inert nature of these surfaces compared to the pristine Mg (0001) surface for electrolyte decomposition. Baskin et.al., used DFT and AIMD simulations to demonstrate the critical role of solvation structure in the reductive stability of the contact-ion pair configurations of Mg(TFSI)2 salt in diglyme solvent[39]. It is clear from these previous studies that atomistic modeling provides a molecular level understanding of the interfacial reactivity of electrolytes to complement and guide experimental observations.

In this paper, we report the results of AIMD simulations performed to *understand the reactivity and decomposition pathways of an electrolyte consisting of 0.5 M $Mg(TFSI)_2$ salt in DME solvent on a pristine Mg (0001) surface*. The effect of the initial structure of the $Mg(TFSI)_2$ salt near *Mg(0001)* surface on the degradation pathway is investigated. We have modeled the interactions of two configurations of the electrolyte with the Mg anode surface: *(i)* a solvent separated ion pair (SSIP) and *(ii)* a contact ion pair (CIP) as shown in **Scheme 1**. The SSIPs and CIPs are likely bulk solvation structures of divalent metal salts in non-aqueous solvents, such as acetonitrile, dimethylsulfoxide (DMSO), 1,2-dimethoxyethane (DME), and tetrahydrofuran (THF), as observed in experiments[40] and classical molecular dynamics (MD) simulations[41]. In the case of the SSIP configuration, the first solvation shell of the cation is composed of multiple solvent molecules, whereas in the CIP configuration, the first solvation shell of the cation consist of a combination of one or more anionic species and multiple solvent molecules[41], as depicted in **Scheme 1**. The relative abundance of the SSIP and CIP configurations in the bulk electrolyte solution is determined by the complex interplay between cation-solvent and cation-anion interaction strengths[40]. In this paper, we report likely decomposition products generated during the initial stages of SEI formation on the Mg anode surface for the two configurations shown in **Scheme 1**. We also report a detailed charge analysis to understand the effect of charge transfer from the Mg (0001) surface on the reactivity of the electrolyte. The technical details of the methodology and simulations are provided in the *Computational Details* section and the simulation results are discussed in the *Results and Discussion* section. We anticipate that the reported atomistic simulations of Mg anode-electrolyte reactivity will be useful for establishing a molecular level understanding of SEI formation and the future development of multivalent battery technology.

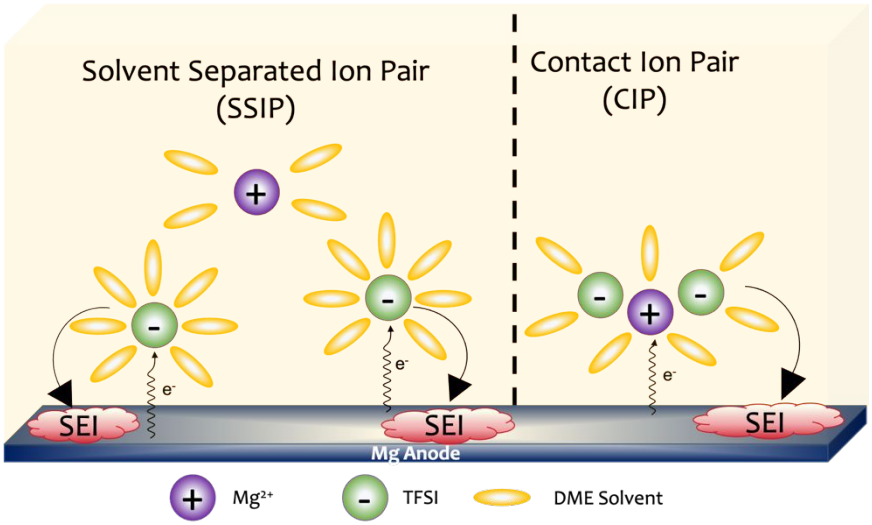

Scheme 1: Schematic representation of the interactions of the solvent separated ion pair (SSIP) and contact ion pair (CIP) configurations of the $Mg(TFSI)_2$ salt in DME solvent with a Mg anode surface. Each configuration undergoes reduction and subsequent chemical transformation at the Mg anode surface to form distinct solid electrolyte interphase (SEI) components.

Computational Details:

All the periodic DFT calculations were performed using the VASP software[42-45]. The exchange-correlation energy was determined using the generalized gradient approximation (GGA) Perdew-Burke-Ernzerhof (PBE)[46] functional coupled with the DFT-D3 method of Grimme *et al*.[47] to account for Van der Waals (vdW) interactions. A plane wave basis set with an energy cutoff of 450 eV was used to expand the electronic wavefunction and projector-augmented wave (PAW)[48],[49],[50] pseudopotentials were used to describe the interactions between core and valence electrons. The Brillouin zone integration was performed using Γ k-point for surface calculations. The ions in the computational cell were allowed to relax until the forces on all the atoms were less than 0.04 eV/Å. The Mg anode was modeled using a 5-layer Mg (0001) surface slab consisting of 6x6 unit cells in the surface plane. A 15 Å vacuum layer was introduced to avoid interaction of the surface plane with the periodic image. The optimized geometry of the 5-layer Mg (0001) surface slab is shown in **Figure 1(a)**.

The reactivity and stability of the liquid-phase electrolyte, consisting of $Mg(TFSI)_2$ as the salt and DME as the solvent, with a pristine Mg (0001) surface was investigated using AIMD simulations. The initial configuration of the liquid-phase electrolyte was generated using the PACKMOL[51] code. The volume of the vacuum region was computed based on the lateral (X and Y) dimensions of the Mg (0001) surface slab (i.e., ~18Å x ~16Å) and the available height of the vacuum region above the surface slab (~12Å) as depicted in Figure 1(a). The electrolyte system is placed such that there is a gap of ~1.5 Å between the top layer of the Mg (0001) surface slab and the electrolyte as well as the periodic image of the bottom layer and the electrolyte to avoid high forces between the atoms of the surface slab and the liquid electrolyte in the initial configuration. The total number of solvent molecules required to fill the volume of the vacuum region were calculated based on the density of DME solvent (0.87 g/cm^3) and molar mass of DME solvent molecule. A total of twenty DME solvent molecules were added to the vacuum region of the surface slab. The $Mg(TFSI)_2$ salt species was then added by replacing 1 DME solvent molecule with 1 $Mg(TFSI)_2$ salt species to achieve a salt concentration of ~0.5 M, consistent with concentrations reported in the literature[52],[53]. The optimized gas-phase structures of the DME solvent molecule and the $Mg(TFSI)_2$ salt species were computed from cluster calculations using the Gaussian 16[54] software at the wb97xd/6-31+G(d,p)[55] level of theory (DFT). The optimized geometries of the $Mg(TFSI)_2$ salt and DME solvent molecule from the cluster calculations are shown in **Figure 1 (b)** and **(c)**, respectively.

We propose three configurations of the liquid electrolyte. The initial model systems of the Mg surface slab in contact with liquid electrolyte in three configurations, consisting of 515 atoms (including atoms of the solvent and salt molecules), were first optimized using periodic DFT. The optimized geometries for the three configurations are shown in Figure 1(d)-(f). The first electrolyte configuration corresponds to a solvent separated ion pair (SSIP), where the Mg^{2+} cation and two TFSI anions do not interact directly with each other and are completely solvated by the DME molecules, as shown in **Figure 1 (d)**. Here, the two TFSI anions are placed closer to

the Mg(0001) surface slab as compared to the Mg^{2+} cation to understand the reactivity and decomposition pathways of TFSI anion species at the Mg anode surface. Recently, Baskin et.al. employed free energy sampling techniques to report that anions and negatively charged contact-ion pairs can reach much closer (~3-4 Å) to the surface of neutral and negatively charged graphene electrode as compared to the divalent cation (~6.5 Å) without experiencing a significant free energy barrier[56]. Such observations justify the relevance of the specific SSIP configuration modeled in this work. The second configuration corresponds to a contact ion pair (CIP), where the Mg^{2+} cation and two TFSI anions are in direct contact with each other, and the $Mg(TFSI)_2$ species is solvated by the DME molecules. We modeled two scenarios for the CIP configuration, denoted as CIP-1 and CIP-2. In the first scenario (CIP-1), the $Mg(TFSI)_2$ species is placed near the Mg(0001) surface as shown in **Figure 1 (e)**. In the second scenario (CIP-2), the $Mg(TFSI)_2$ species is placed relatively far from the surface (~8 Å from top surface layer) as shown in **Figure 1 (f)** to study the effect of proximity of the anode surface on the reactivity of the salt. The two TFSI anions in the salt species, denoted here as TFSI-1 and TFSI-2, are marked using blue and red boxes, respectively, for identification and discussion of the reaction mechanism of each anion species.

AIMD simulations were carried out using the optimized structures with a time step of 1 fs for a total duration of 10 ps. We replaced the mass of the hydrogen atoms of the DME solvent molecules with the mass of tritium to achieve higher time steps, consistent with the literature[31]. All the AIMD simulations were carried out using Γ k-point. The AIMD simulations were performed using NVT ensemble at a temperature of 750 K. The temperature oscillations during the AIMD simulations are controlled using the Nose thermostat. The variation of the temperature as a function of time for the three AIMD simulations (SSIP, CIP-1 and CIP-2) are shown in Figure S1 of the supplementary information. We performed additional benchmarking AIMD simulations using the SSIP configuration of the $Mg(TFSI)_2$ species at lower temperatures of 350 K and 650 K, as discussed in the *Results and Discussion* section. We also performed Bader charge analysis[57-60] to understand the effect of charge transfer on the stability of the electrolyte during the AIMD simulations. The Bader charges of all the atoms of the TFSI anions (TFSI-1 and TFSI-2), DME solvent, and Mg surface slab were computed as a function of time for the entire trajectory of the AIMD simulations.

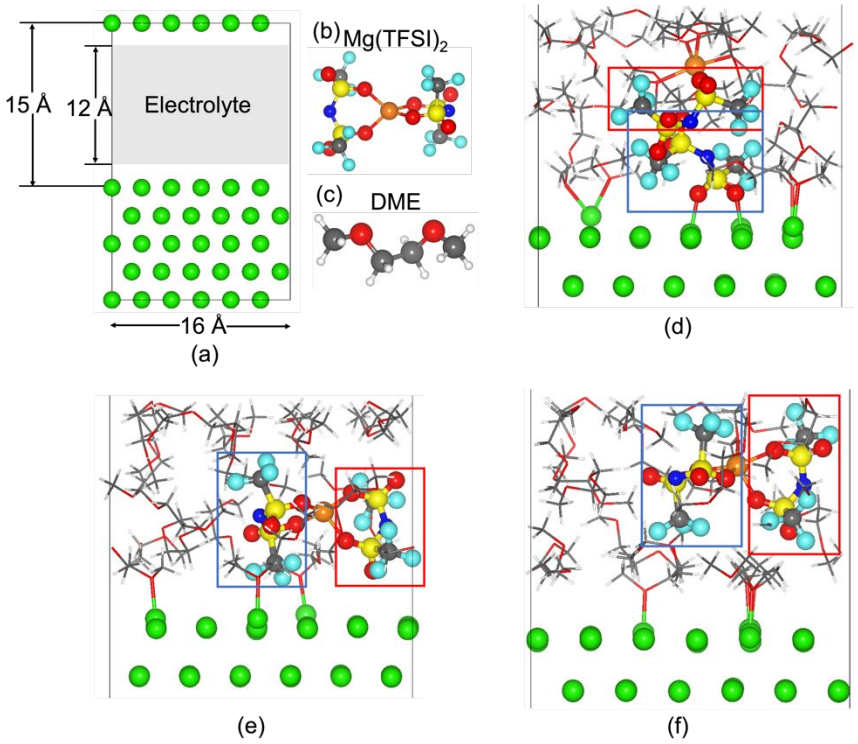

Figure 1: Optimized geometry of (a) pristine Mg (0001) surface slab, (b) $Mg(TFSI)_2$ salt, and (c) DME solvent molecule. Optimized geometries of Mg (0001) surface slab in contact with electrolyte (0.5 M $Mg(TFSI)_2$ salt in dimethoxy ethane (DME) solvent) in (d) solvent separated ion pair (SSIP) configuration, (e) contact ion pair (CIP-1) configuration where $Mg(TFSI)_2$ salt is placed near the surface, (f) contact ion pair (CIP-2) configuration where $Mg(TFSI)_2$ salt is placed at a distance of ~8 Å from the top layer of the surface. The TFSI-1 and TFSI-2 anions are marked using blue and red boxes, respectively. The color codes for the atoms are: green: surface Mg, orange: salt Mg, red: O, yellow: S, blue: N, grey: C, cyan: F and white: H. The salt and solvent molecules in (d)-(f) are shown using ball-stick and stick representations, respectively.

Results and Discussion:

Solvent Separated Ion Pair (SSIP) Configuration:

The reactivity of the electrolyte (0.5 M $Mg(TFSI)_2$ salt in DME solvent) with the pristine Mg (0001) surface was studied using AIMD simulations to understand the degradation reaction mechanisms and the key SEI products formed during the initial stages of electrolyte decomposition on the anode surface. Our first step was to determine a suitable temperature for the AIMD simulations to observe electrolyte degradation reactions within the limited duration of the AIMD simulations (*i.e.,* 10 ps*)*. Thus, we performed benchmarking simulations using the SSIP configuration of the $Mg(TFSI)_2$ salt at three different initial temperatures (350, 650, and 750 K) below the melting point of Mg (T_m of Mg metal is 923 K) for 10 ps each. At temperatures of 350 and 650 K, we did not observe reaction between the salt or the solvent molecules and the anode surface within the time frame of the AIMD simulations (see Figure S2 (a) and (b), respectively in

the supplementary material). However, at 750 K one of the two TFSI anions undergoes rapid bond dissociation reactions forming various degradation products on the Mg (0001) (see Figure S2 (c)). In order to investigate the thermal stability of the electrolyte, we performed two additional AIMD simulations of the SSIP configuration of the bulk electrolyte system without the Mg (0001) surface slab at temperatures of 350 K and 750 K for 10 ps each. The electrolyte is observed to be thermally stable at both the temperatures within 10 ps of the AIMD simulations as shown by the initial (t = 0 ps) and final (t = 10 ps) configurations of the electrolyte system at temperatures of 350 K and 750 K in Figure S3 of the supplementary information. We also compared the radial distribution functions (RDFs) of the final configurations of the bulk electrolyte (after 10 ps AIMD simulation) at 350 K and 750 K to understand the effect of temperature on the bulk solvation structure of the electrolyte as discussed in Figure S4 of the supplementary information. Based on this initial examination, all the subsequent AIMD simulations reported in this work were performed at a temperature of 750 K for a duration of 10 ps.

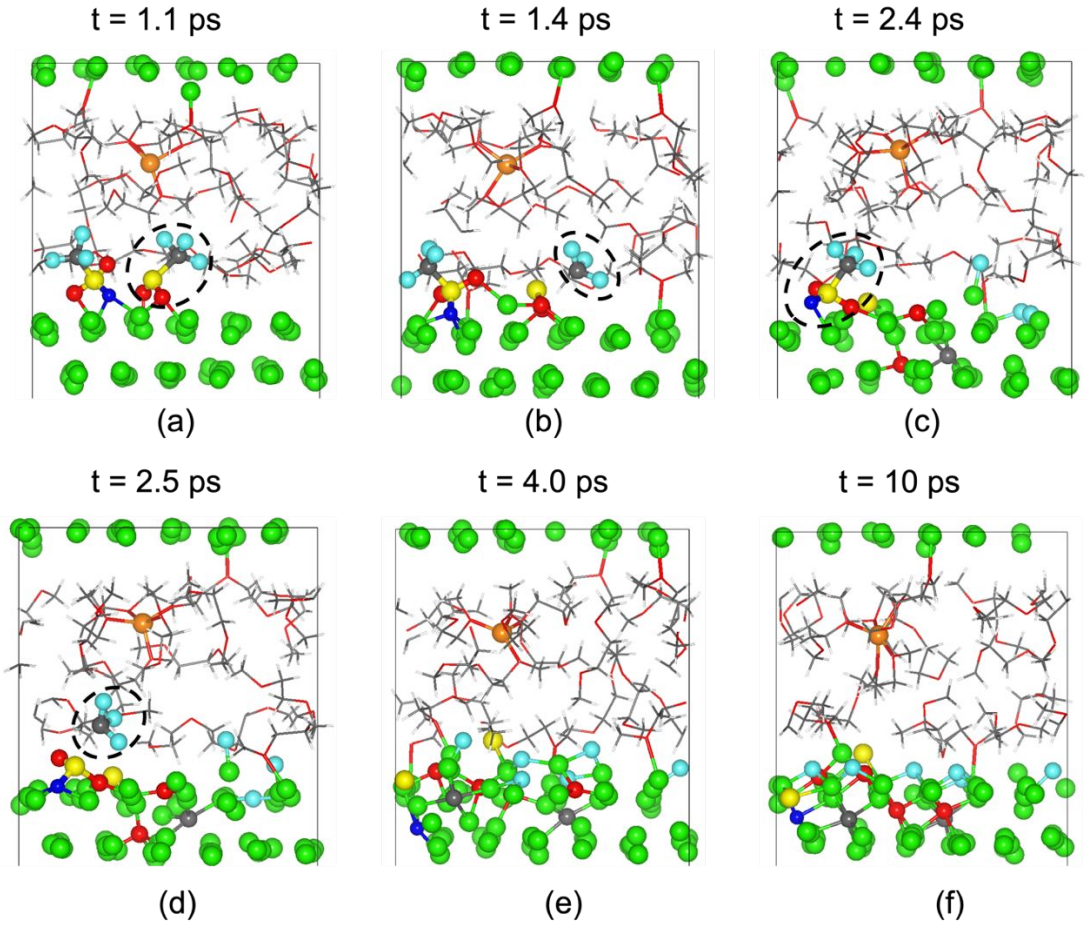

Figure 2: (a)-(f) Six representative snapshots at various times (*t*) from AIMD simulation at 750 K showing the reductive reaction pathway of $Mg(TFSI)_2$ species in DME solvent in the SSIP configuration on the Mg(0001) surface. The color code of the atoms is the same as described in Figure 1. Selected molecular fragments in each snapshot are marked by dashed black circles to show their presence.

Six representative snapshots of the $Mg(TFSI)_2$ species in the SSIP configuration depicting the chemical transformation of the TFSI-1 anion during the simulation are shown in **Figure 2 (a)-(f)**. The TFSI-2 anion of the $Mg(TFSI)_2$ species is not shown here for clarity and its structural transformations are discussed separately in Figure S2. As shown in **Figure 2 (a)**, the first step in the dissociation reaction pathway is cleavage of the N-S bond of the TFSI-1 moiety at ~1.1 ps resulting in the formation of NSO_2CF_3 and SO_2CF_3 (the latter marked by a dashed black circle) fragments. Subsequently, as shown in **Figure 2(b),** dissociation of the C-S bond of the SO_2CF_3 fragment forms SO_2 and CF_3 fragments at a time of ~1.4 ps. Note that the CF_3 fragment is marked by a dashed black circle. Within the next 1 ps, the CF_3 and SO_2 fragments dissociate into individual elemental components (*i.e.,* C, F, S, and O atoms) which remain adsorbed on the Mg anode surface, as shown in **Figure 2(c)**. The CF_3 fragment undergoes 3 sequential and spontaneous C-F bond dissociation reactions forming CF_2, CF, and a C atom, respectively. As shown in **Figure 2(d)**, the remaining NSO_2CF_3 fragment starts to dissociate *via* cleavage of the C-S bond, forming another CF_3 fragment (shown by a dashed black circle) and NSO_2 fragment at 2.5 ps. Within the next 1.5 ps, the CF_3 and NSO_2 fragments dissociate into their elemental components *via* cleavage of C-F, S-O, and N-S bonds, as shown in **Figure 2(e)**. The resulting elemental constituents (*i.e.,* C, F, S, O, and N atoms) stay adsorbed on the Mg surface for the remaining simulation time, as shown in **Figure 2(f)**. It should be noted that the O and C atoms intercalate into the subsurface layer of the Mg slab forming a network of MgO and MgC species. In comparison, the S and F atoms remain adsorbed on the top layer of the Mg (0001) surface resulting in formation of MgF_2 and MgS species. Thus, the TFSI-1 anion undergoes complete dissociation within ~4 ps of simulation time at 750 K. The TFSI-2 anion of the $Mg(TFSI)_2$ species remains stable for the entire duration of the simulation, as shown by the initial (at t = 0 ps) and final (at t = 10 ps) configurations of the TFSI-2 anion (Figure S5). Additionally, the DME solvent molecules remain stable and do not undergo any degradation reaction with the Mg anode surface during 10 ps of AIMD simulation. We note that the DME solvent molecules have been reported to be stable in previous AIMD simulations of electrolyte reactivity with Li metal anodes in Li-S batteries[31],[30]. Detailed movies showing the entire AIMD simulation of the reductive reaction of the TFSI-1 and TFSI-2 anions of $Mg(TFSI)_2$ in the SSIP configuration are provided in movies S1 (a) and (b), respectively of the supplementary material. We performed an additional AIMD simulation of the SSIP configuration of the electrolyte where Mg^{2+} cation and the two TFSI anions are placed near and far from the Mg (0001) surface slab, respectively to investigate the effect of the proximity of surface on reactivity of TFSI anions. The AIMD simulation is carried out for a total duration of 5 ps. The comparison of the initial (t = 0 ps) and final configurations (t = 5 ps) of the system (see Figure S6 of the supplementary information) shows that TFSI anions remain stable and do not undergo decomposition reaction within 5 ps of AIMD simulations. It is clear from the simulation that the electron transfer from the Mg (0001) surface slab drives the reductive decomposition of TFSI anions at the anode surface and longer duration AIMD simulations are needed to study the reactivity of TFSI anions which are located away from the anode surface.

Contact Ion Pair (CIP-1) Configuration:

Snapshots of the electrolyte in the CIP-1 configuration at different times during the AIMD simulation, depicting the degradation reaction mechanism of the TFSI-1 molecule, are shown in **Figure 3(a)-(f).** For clarity, the TFSI-2 molecule is not shown in the snapshots and its decomposition mechanism is discussed separately (see Figure S3). The starting complex is shown in **Figure 3(a)**. As shown in **Figure 3(b**), the first bond dissociation reaction for the TFSI-1 anion is the cleavage of the S-CF_3 bond at a time of ~0.2 ps resulting in formation of the CF_3 fragment (marked by a dashed black circle) which adsorbs on the Mg (0001) surface. The CF_3 fragment is highly reactive and rapidly dissociates into a C atom and three F atoms *via* three sequential C-F bond dissociation reactions. The C atom migrates to the subsurface layer of the Mg anode while the F atoms form a network of MgF_2 species. Within the next ~1 ps, another CF_3 fragment (marked by a dashed black circle) forms *via* a second S-CF_3 bond dissociation reaction, as shown in **Figure 3(c)**. This CF_3 fragment is released away from the Mg anode surface and remains solvated by DME molecules for the duration of the AIMD simulation without undergoing further reaction. Thus, it is clear that rapid dissociation of the CF_3 fragment into C and F atoms *via* C-F bond dissociation reactions is triggered by direct interaction of the CF_3 fragment with the Mg (0001) surface. Decomposition of the remaining $N(SO_2)_2$ fragment *via* N-S and multiple S-O bond dissociation reactions, leading to formation of NSO species (shown by a dashed black circle), is shown in **Figure 3(d).** The O atoms react with the Mg surface to form a MgO network. The NSO fragment remains stable for the next ~5 ps of the AIMD simulation before dissociating into individual elemental constituents, (*i.e.,* N, S, and O atoms) *via* cleavage of S-O and N-S bonds, as shown in **Figure 3(e).** No further reactions occur among the elemental species for the duration of the simulation, as shown in **Figure 3(f).**

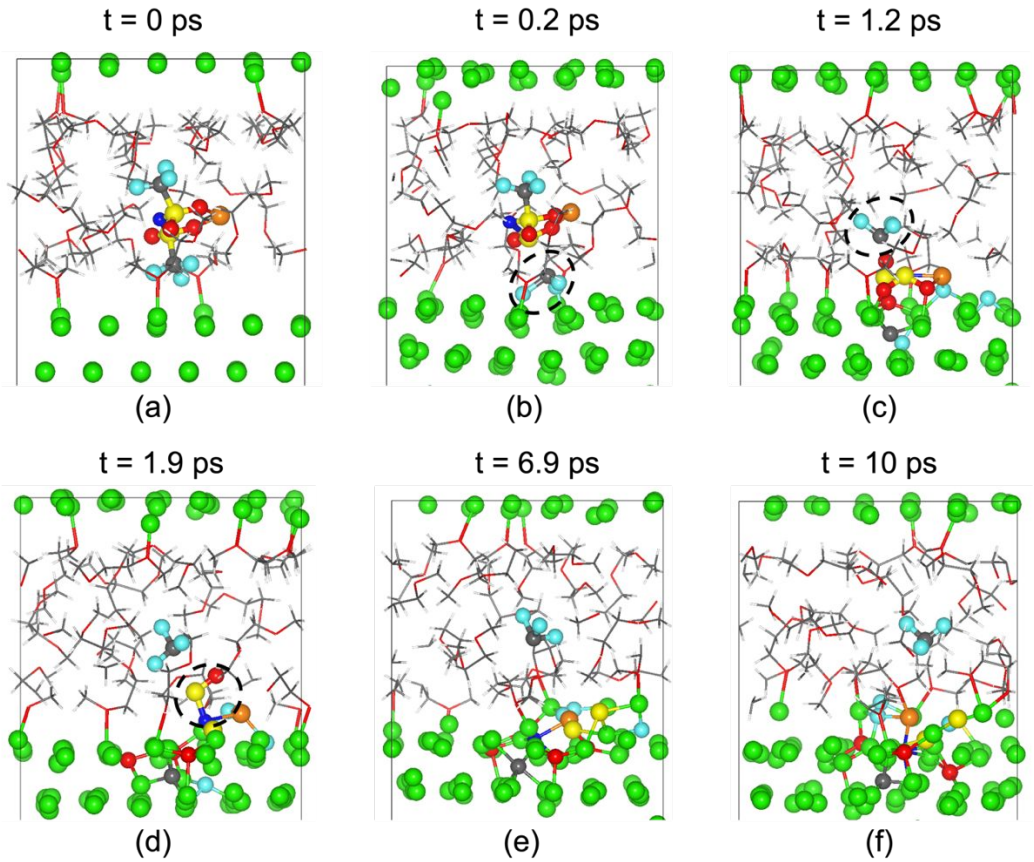

Figure 3: (a)-(f) Six representative snapshots at various times (*t*) from AIMD simulation at 750 K showing the reductive reaction pathway of the TFSI-1 anion of $Mg(TFSI)_2$ in the CIP-1 configuration on a Mg(0001) surface. The color code of the atoms is the same as described in Figure 1. Selected molecular fragments in each snapshot are marked by dashed black circles to show their presence.

The decomposition reaction mechanism of the second TFSI anion (TFSI-2) is similar to the TFSI-1 degradation pathway described above. Representative snapshots depicting the reductive reaction mechanism of the TFSI-2 anion are shown in Figure S7(a)-(f). The decomposition of the TFSI-2 anion also starts *via* cleavage of the S-CF_3 bond at ~3 ps. However, the TFSI-2 anion does not undergo complete dissociation into its elemental constituents within 10 ps of AIMD simulation. Similar to the SSIP case (**Figure 2**), the DME solvent molecules in CIP-1 remain stable and do not undergo reduction reaction with the Mg (0001) surface during the time frame of the AIMD simulation. Detailed movies showing the entire AIMD simulation of the reduction reactions of the TFSI-1 and TFSI-2 anions of $Mg(TFSI)_2$ species in the CIP-1 configuration are provided in movies S2 (a) and (b), respectively, of the supplementary material.

Contact Ion Pair (CIP-2) Configuration:

We also performed AIMD simulations to probe the effect of the proximity of the Mg surface on the reactivity of the $Mg(TFSI)_2$ salt species in the CIP configuration. In CIP-2 configuration, we placed the $Mg(TFSI)_2$ species at a distance of ~8 Å from the top layer of the Mg (0001) surface (**Figure 1(f)**). In this scenario, the $Mg(TFSI)_2$ species do not undergo extensive decomposition compared to the two previous cases (**Figure 2 & 3**) where $Mg(TFSI)_2$ was placed adjacent to the surface. Snapshots of the simulation depicting the reaction mechanism of the TFSI-1 anion in the CIP-2 configuration are presented in **Figure 4**. The TFSI-2 anion of the $Mg(TFSI)_2$ species is not shown for clarity. The TFSI-2 anion does not undergo a reduction reaction with the Mg surface and remains stable for the entire duration of the simulation, as shown by the initial (at t = 0 ps) and final (at t = 10 ps) snapshots (see Figure S8). In **Figure 4(a)**, the initial complex at t = 0 ps is shown. In **Figure 4(b)**, the TFSI-1 anion loses a CF_3 group (marked by a dashed black circle) at ~0.3 ps *via* cleavage of the S-CF_3 bond. As shown in **Figure 4(c)-(e),** the CF_3 group further reacts with the Mg (0001) surface and dissociates into C and three F atoms *via* three sequential C-F bond dissociation reactions within ~0.3 ps. The CF_2 and CF groups are highlighted by dashed black circles in **Figure 4(c),(d)**, respectively. The three F atoms and the C atom remain adsorbed on the surface for the duration of the simulation. As shown in **Figure 4(f)**, the rest of the salt molecule remains stable and does not undergo further decomposition within 10 ps of simulation. Similar to the previous cases (**Figure 2:** SSIP and **Figure 3:** CIP-1), the DME solvent molecules remain stable for the entire duration of the AIMD simulation. Based on these simulations, the Mg (0001) surface plays a critical role in driving the decomposition reaction of $Mg(TFSI)_2$ species in DME solvent. Similar behavior has been reported for the LiTFSI salt in previous AIMD simulations where LiTFSI undergoes limited decomposition when placed relatively far from the Li metal anode surface[31]. Detailed movies showing entire AIMD simulations of the reduction reactions of the TFSI-1 and TFSI-2 anions of $Mg(TFSI)_2$ in the CIP-2 configuration are provided in movies S3(a,b), respectively of the supplementary material.

It is clear from these AIMD simulations that the initial configuration of the $Mg(TFSI)_2$ species near the Mg anode surface impacts the degradation reaction mechanism and the extent of TFSI decomposition. For example, dissociation of the $Mg(TFSI)_2$ species in the SSIP and both CIP configurations begins *via* cleavage of the N-S and C-S bonds of the TFSI anion, respectively. This is in agreement with the trend of DFT computed bond dissociation energies reported in the literature[41], where the C-S bond dissociation reaction becomes thermodynamically favorable when the TFSI anion is paired with a partially reduced Mg^+ cation. Furthermore, the first C-S bond cleavage reaction in both CIP configurations is more rapid (~0.2-0.3 ps) compared to the first N-S bond cleavage reaction (~1.1 ps) in the SSIP configuration.

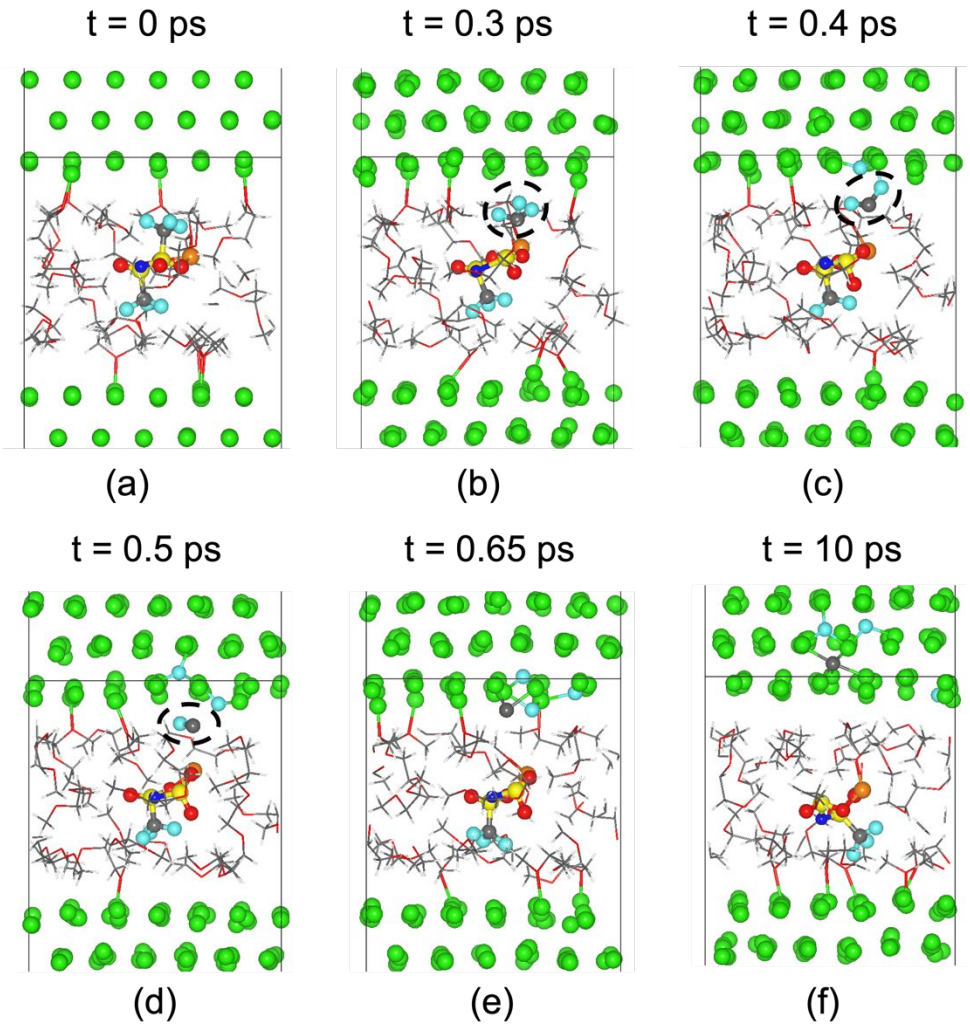

Figure 4: (a)-(f) Representative snapshots from AIMD simulation at 750 K showing the reduction reaction pathway of $Mg(TFSI)_2$ salt in the CIP-2 configuration on a Mg(0001) surface. The color code of the atoms is the same as described in Figure 1. Selected molecular fragments in each snapshot are marked by dashed black circles to show their presence.

Bader Charge Analysis:

To understand the role of charge transfer in the stability of the electrolyte, we performed Bader charge analyses for every 100 fs step during the AIMD simulations. The Bader charges were computed for each atom of $Mg(TFSI)_2$, the DME molecule, and the Mg surface slab. In **Figure 5(a)**, the net per-atom charge transferred from the Mg (0001) surface slab to the $Mg(TFSI)_2$ species in the SSIP (red line), CIP-1 (blue line), and CIP-2 (green line) configurations is compared. The reference is defined as the Bader charges of the Mg atoms of the surface slab at 0 ps. In the SSIP configuration, charge transfer from the Mg surface slab starts at ~1 ps, coinciding with the first N-S bond cleavage reaction, as described in **Figure 2(a).** The charge transfer continues until ~4 ps, after which the net charge of the Mg surface slab saturates at a value of ~24 *e*/atom for the remainder of the simulation (see red line). This observation is consistent with the various

decomposition reactions described in **Figure 2**, where the TFSI-1 molecule adjacent to the metal surface undergoes complete dissociation into its elemental constituents within ~4 ps of AIMD simulation time. The TFSI-2 molecule does not undergo a degradation reaction with the Mg surface within the simulation time. In the case of the CIP-1 configuration of the $Mg(TFSI)_2$ species, charge transfer from the Mg slab starts at t = ~200 fs, as shown by the blue line (larger slope than the other red or green lines) in **Figure 5(a)**. This rapid charge transfer results in instantaneous dissociation of the S-CF_3 bond of the TFSI-1 anion, as shown in **Figure 3(b)**. Here, a total charge of ~34 *e*/atom is transferred from the Mg (0001) surface to the electrolyte during 10 ps of AIMD simulation time. The larger charge transfer leads to dissociation of both the TFSI-1 and TFSI-2 anions of the $Mg(TFSI)_2$ salt, compared to dissociation of only one TFSI anion (TFSI-1) in the SSIP configuration. In the CIP-2 configuration, where the $Mg(TFSI)_2$ salt species is placed further away from the surface, the net charge of the Mg surface slab saturates at a value of ~6 *e*/atom within ~1 ps of the AIMD simulation, as shown by the green line in **Figure 5(a)**. The initial charge transfer from the Mg surface results in dissociation of the S-CF_3 bond of the TFSI-1 anion, as shown earlier in **Figure 4(b)**. No additional electron transfer occurs between the Mg (0001) surface and the $Mg(TFSI)_2$ species for the remainder of the simulation. Thus, the limited reactivity of the $Mg(TFSI)_2$ species in the CIP-2 configuration is attributed to the small number of electrons transferred from the Mg (0001) surface. Thus, the interaction of the $Mg(TFSI)_2$ species with the Mg surface facilitates charge transfer from the anode surface to the salt species that drives the decomposition reactions.

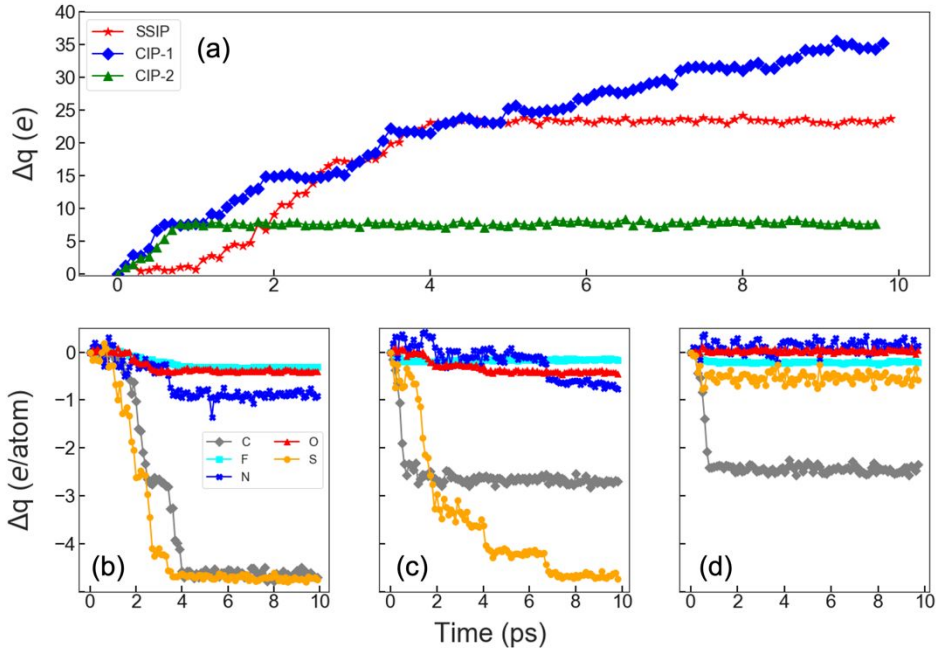

Figure 5: Temporal evolution of the change in per-atom Bader charges (Δq, *e*/atom) of (a) Mg (0001) surface slab, atomic species of the TFSI-1 anion of $Mg(TFSI)_2$ species in the (b) SSIP, (c) CIP-1, and (d) CIP-2 configurations during 10 ps of AIMD simulation time. The reference is taken as the Bader charges of the atoms at 0 ps

The extent of charge transfer from the metal surface to the electrolyte is critical to the spontaneous chemical reactivity observed during the dynamic simulations. For a detailed

analysis, we investigated the net per-atom charge transferred to each atomic species of the TFSI-1 anion in the $Mg(TFSI)_2$ species in the SSIP, CIP-1, and CIP-2 configurations. The reference is defined as the charge of atoms of the TFSI-1 anion at 0 ps. The results are shown in **Figures 5(b-d),** respectively. Similarly, the per-atom charges of the atomic species of the TFSI-2 anion as a function of time for the three configurations are shown in Figure S9(a-c) of the supplementary material. In **Figure 5(b)**, the majority of the charge is transferred to the C (~-5 *e*/atom) and S (~-5 *e*/atom) atoms of the TFSI-1 anion from the Mg (0001) surface in the SSIP configuration. The higher amount of charge transferred to the C and S atoms is attributed to complete dissociation of the TFSI-1 anion into its elemental constituents (i.e., C, S, O, N, F) which gets adsorbed on the surface of Mg (0001) slab within 10ps duration of AIMD simulation. The S atom of the TFSI-1 anion starts to gain electrons from the Mg (0001) surface at ~1 ps. This initial charge transfer to the S atom triggers cleavage of the N-S bond of the TFSI-1 anion at ~1 ps, as previously shown in **Figure 2(a)**. In comparison, only a small number of electrons (-0.6 *e*/atom, -0.3 *e*/atom, and -0.23 *e*/atom) are transferred to the N, O, and F atoms during 10 ps of AIMD simulation time. In comparison, the net atomic charges of the TFSI-2 anion oscillate around a constant value of ~0 *e*/atom (see Figure S9(a) of the supplementary material) indicating lack of charge transfer from the Mg (0001) surface to the atoms of the TFSI-2 anion. Thus, the TFSI-2 anion remains stable and does not undergo any degradation reaction with the Mg (0001) surface.

In the case of the CIP-1 configuration, instantaneous charge transfer to the C and S atoms of the TFSI-1 anion triggers cleavage of the S-CF_3 bond at ~0.2 ps. The C and S atoms of the TFSI-1 anion gain a total charge of ~-3 *e*/atom and ~-5 *e*/atom, respectively, within 10 ps of AIMD simulation time, as shown in **Figure 5(c).** The smaller number of electrons gained by the C atoms of the TFSI-1 anion in the CIP-1 configuration is attributed to the formation of a stable solvated CF_3 fragment, which does not undergo a reduction reaction with the Mg surface, as described in **Figure 3**. In addition, the C and S atoms of the TFSI-2 anion in the CIP-1 configuration start to gain electrons from the Mg (0001) surface at ~3 ps (see Figure S9(b) of the supplementary material). This charge transfer to the C and S atoms leads to the first S-CF_3 bond dissociation reaction of the TFSI-2 anion at a time of ~3 ps. A total charge of ~-4 *e*/atom and ~-3 *e*/atom is transferred to the C and S atoms, respectively, of the TFSI-2 anion within 10 ps of AIMD simulation time. Thus, both of the TFSI anions (TFSI-1 and TFSI-2) of the $Mg(TFSI)_2$ species gain electrons from the Mg(0001) surface in the CIP-1 configuration, compared to one TFSI anion (TFSI-1) in the SSIP configuration.

In the CIP-2 configuration, where the $Mg(TFSI)_2$ salt is placed further away from the surface (~8 Å), instantaneous charge transfer occurs between the Mg(0001) surface and the C atom of the TFSI-1 anion (within 1 ps of AIMD simulation time), as shown in **Figure 5(d)**. The net Bader charge of ~-2.5 *e*/atom is transferred to the C atom of the TFSI-1 anion. The initial charge transfer triggers the S-CF_3 bond dissociation reaction leading to formation of the CF_3 fragment (which dissociates into its elemental constituents, *i.e.,* C and three F atoms), as described in **Figure 4**. No further charge transfer occurs between the Mg (0001) surface and the TFSI-1 anion. The charges of the atomic species of the TFSI-2 anion oscillate around ~0 *e*/atom (shown in Figure S9(c)), suggesting no net charge transfer between the Mg (0001) surface and the atoms of the TFSI-2 anion during the AIMD simulation. Similarly, the atomic charges of the C and O atoms of the DME solvent molecules for the three configurations of the $Mg(TFSI)_2$ salt as a function of time, are shown in Figure S10(a)-(c), respectively. The net change in Bader charges of the C and O atoms oscillate around average values of ~-0.5 *e*/atom and ~0.5 *e*/atom, respectively, for the

entire duration of the AIMD simulations of the $Mg(TFSI)_2$ species in the SSIP, CIP-1, and CIP-2 configurations. The stability of the DME molecules against reduction reaction with the Mg (0001) surface is attributed to lack of charge transfer between the surface and the solvent molecules. The various bond dissociation reactions and the final fragments formed for each configuration of the $Mg(TFSI)_2$ species are summarized in **Table 1**.

Table 1: Summary of important chemical events and total per-atom charge transferred (Δq, *e*/atom) to the TFSI anions of the $Mg(TFSI)_2$ species during AIMD simulations of reductive degradation reactions of electrolyte on the Mg (0001) surface. Note: * indicate adsorbed species on the anode surface. SSIP and CIP denote solvent separated ion pair and contact ion pair, respectively.

Observation	SSIP (Figure 2)		CIP-1 (Figure 3)		CIP-2 (Figure 4)	
	TFSI-1	TFSI-2	TFSI-1	TFSI-2	TFSI-1	TFSI-2
First Bond Cleavage	N-S (~1.1 ps)	None	C-S (~0.2 ps)	C-S (~3 ps)	C-S (~0.3 ps)	None
Other Bond Cleavage	C-S, C-F, S-O	None	C-F, S-O, N-S	C-F, N-S, S-O	C-F	None
Final Fragments	F*, C*, N*, S*, O*	None	CF_3, F*, C*, N*, S*, O*	NSO_2C, C*, F*, S*, O*	C*, F*, $CF_3SO_2NSO_2$	None
Δq (*e*/atom)	~-1.53	~0	~-1.13	~-1.07	~-0.47	~0

Conclusions

In this contribution, we investigated the interaction of the Mg (0001) surface with an electrolyte consisting of 0.5 M $Mg(TFSI)_2$ salt species in 1,2-dimethoxyethane (DME) solvent using Ab Initio Molecular Dynamics (AIMD) simulations to gain atomic level insights into spontaneous interphase formation on pristine Mg anode surfaces. Based on the simulations, the initial degradation reactions of the electrolyte strongly depend on the initial structure of the $Mg(TFSI)_2$ species near the anode surface. Dissociation of the $Mg(TFSI)_2$ species in the SSIP and CIP (CIP-1 and CIP-2) configurations begins *via* cleavage of the N-S and C-S bonds of the TFSI anion,

respectively. Additionally, the first C-S bond cleavage reaction in the CIP configurations (CIP-1 and CIP-2) is more rapid (~0.2 - 0.3 ps) compared to the first N-S bond cleavage reaction of the TFSI anion in the SSIP configuration (~1.1 ps). In the case of the CIP-1 configuration, both TFSI anions of the $Mg(TSFI)_2$ species undergo degradation reactions. In comparison, only one of the TFSI anions (TFSI-1) undergoes bond dissociation reactions for the SSIP and CIP-2 configurations. The decomposition reactions result in formation of atomic O, C, S, F, and N species adsorbed on the surface of the Mg anode. These products indicate that the initial SEI layer formed on the surface of the pristine Mg anode consists of a complex mixture of multiple components such as oxides, carbides, sulfides, fluorides, and nitrides. The higher reactivity and extensive decomposition of $Mg(TFSI)_2$ species in the CIP-1 configuration is attributed to higher Bader charge transferred from the Mg anode surface (~0.19 *e*/atom) during the decomposition reaction pathway. In comparison, total charges of ~0.13 *e*/atom and ~0.03 *e*/atom are transferred to the salt species in the SSIP and CIP-2 configurations, respectively, from the Mg anode surface during 10 ps of AIMD simulation time. We anticipate that the atomic level insights gained from these molecular simulations will lay the groundwork for the design of tailored and functional interphases which are critical for the future success of multivalent battery technology.

Associated Content

Supporting Information: The supporting material includes additional AIMD snapshots for the reduction reaction of 0.5M $Mg(TFSI)_2$ salt species in DME solvent on the Mg (0001) surface at different temperatures (350, 650, and 750 K). AIMD snapshots and Bader charge analysis of the reduction reaction of the TFSI-2 anion of the $Mg(TFSI)_2$ species in the SSIP, CIP-1, and CIP-2 configurations. Six AIMD simulation movies showing the reduction reaction of the TFSI-1 and TFSI-2 anions of the $Mg(TFSI)_2$ species in the SSIP, CIP-1, and CIP-2 configurations on the Mg (0001) surface.

Author Information

Corresponding Authors

Rajeev S. Assary – *Materials Science Division, Argonne National Laboratory, Lemont, IL, USA, 60439*; orcid.org/0000-0002-9571-3307; *Phone: 630-252-3536; Email: assary@anl.gov*
Garvit Agarwal - *Materials Science Division, Argonne National Laboratory, Lemont, IL, USA, 60439*; orcid.org/0000-0002-1896-1024, Email: garvit.iitr@gmail.com

Authors
Jason Howard - *Materials Science Division, Argonne National Laboratory, Lemont, IL, USA, 60439*; orcid.org/0000-0003-1460-9004

Grant E. Johnson – *Physical Science Division, Pacific Northwest National Laboratory, Richland*, WA, USA; orcid.org/0000-0003-3352-4444
Venkateshkumar Prabhakaran – *Physical Science Division, Pacific Northwest National Laboratory, Richland*, WA, USA; orcid.org/0000-0001-6692-6488
Vijay Murugesan- *Pacific Northwest National Laboratory, Richland*, WA; USA, orcid.org/0000-0001-6149-1702
Karl T. Mueller, *Pacific Northwest National Laboratory, Richland*, WA, USA; orcid.org/0000-0001-9609-9516
Larry A. Curtiss - *Materials Science Division, Argonne National Laboratory, Lemont, IL, USA, 60439*; orcid.org/0000-0001-8855-8006

Author contributions:

GA and RSA conceived the idea and directed the research. GA and JH performed simulations. GA, JH, LAC, VP, GJ, VM, KM, and RSA discussed and analyzed results.

Notes:
The authors declare no competing financial interest.

Acknowledgement
This work was supported by the Joint Center for Energy Storage Research (JCESR), an Energy Innovation Hub funded by the U.S. Department of Energy, Office of Science, Basic Energy Sciences. This research used resources of the National Energy Research Scientific Computing Center; a DOE Office of Science User Facility supported by the Office of Science of the U.S. Department of Energy under Contract No. DE-AC02-05CH11231. We also acknowledge a generous grant of computer time from the Argonne National Laboratory Computing Resource Center (LCRC-Bebop).

References

(1) Trahey, L.; Brushett, F. R.; Balsara, N. P.; Ceder, G.; Cheng, L.; Chiang, Y.-M.; Hahn, N. T.; Ingram, B. J.; Minteer, S. D.; Moore, J. S.; Mueller, K. T.; Nazar, L. F.; Persson, K. A.; Siegel, D. J.; Xu, K.; Zavadil, K. R.; Srinivasan, V.; Crabtree, G. W. Energy Storage Emerging: A Perspective from the Joint Center for Energy Storage Research. *Proceedings of the National Academy of Sciences* **2020,** *117* (23), 12550, DOI: 10.1073/pnas.1821672117.
(2) Thackeray, M. M.; Wolverton, C.; Isaacs, E. D. Electrical Energy Storage for Transportation—Approaching the Limits of, and Going Beyond, Lithium-ion Batteries. *Energy & Environmental Science* **2012,** *5* (7), 7854-7863, DOI: 10.1039/C2EE21892E.
(3) Dunn, B.; Kamath, H.; Tarascon, J.-M. Electrical Energy Storage for the Grid: A Battery of Choices. *Science* **2011,** *334* (6058), 928-935, DOI: 10.1126/science.1212741.

(4) Tian, Y.; Zeng, G.; Rutt, A.; Shi, T.; Kim, H.; Wang, J.; Koettgen, J.; Sun, Y.; Ouyang, B.; Chen, T.; Lun, Z.; Rong, Z.; Persson, K.; Ceder, G. Promises and Challenges of Next-Generation "Beyond Li-Ion" Batteries for Electric Vehicles and Grid Decarbonization. *Chemical Reviews* **2020**, DOI: 10.1021/acs.chemrev.0c00767.
(5) Mohtadi, R.; Mizuno, F. Magnesium batteries: Current State of the Art, Issues and Future Perspectives. *Beilstein Journal of Nanotechnology* **2014,** *5*, 1291-1311, DOI: 10.3762/bjnano.5.143.
(6) Saha, P.; Datta, M. K.; Velikokhatnyi, O. I.; Manivannan, A.; Alman, D.; Kumta, P. N. Rechargeable Magnesium Battery: Current Status and Key Challenges for the Future. *Progress in Materials Science* **2014,** *66*, 1-86, DOI: https://doi.org/10.1016/j.pmatsci.2014.04.001.
(7) Deivanayagam, R.; Ingram, B. J.; Shahbazian-Yassar, R. Progress in Development of Electrolytes for Magnesium Batteries. *Energy Storage Materials* **2019,** *21*, 136-153, DOI: https://doi.org/10.1016/j.ensm.2019.05.028.
(8) Qu, X.; Zhang, Y.; Rajput, N. N.; Jain, A.; Maginn, E.; Persson, K. A. Computational Design of New Magnesium Electrolytes with Improved Properties. *The Journal of Physical Chemistry C* **2017,** *121* (30), 16126-16136, DOI: 10.1021/acs.jpcc.7b04516.
(9) Yu, X.; Manthiram, A. Electrode–Electrolyte Interfaces in Lithium-Based Batteries. *Energy & Environmental Science* **2018,** *11* (3), 527-543, DOI: 10.1039/C7EE02555F.
(10) Wang, A.; Kadam, S.; Li, H.; Shi, S.; Qi, Y. Review on Modeling of the Anode Solid Electrolyte Interphase (SEI) for Lithium-Ion Batteries. *npj Computational Materials* **2018,** *4* (1), 15, DOI: 10.1038/s41524-018-0064-0.
(11) Lu, Z.; Schechter, A.; Moshkovich, M.; Aurbach, D. On the Electrochemical Behavior of Magnesium Electrodes in Polar Aprotic Electrolyte Solutions. *Journal of Electroanalytical Chemistry* **1999,** *466* (2), 203-217, DOI: https://doi.org/10.1016/S0022-0728(99)00146-1.
(12) Wetzel, D. J.; Malone, M. A.; Haasch, R. T.; Meng, Y.; Vieker, H.; Hahn, N. T.; Gölzhäuser, A.; Zuo, J.-M.; Zavadil, K. R.; Gewirth, A. A.; Nuzzo, R. G. Passivation Dynamics in the Anisotropic Deposition and Stripping of Bulk Magnesium Electrodes During Electrochemical Cycling. *ACS Applied Materials & Interfaces* **2015,** *7* (33), 18406-18414, DOI: 10.1021/acsami.5b04487.
(13) Yoo, H. D.; Shterenberg, I.; Gofer, Y.; Gershinsky, G.; Pour, N.; Aurbach, D. Mg Rechargeable Batteries: An On-going Challenge. *Energy & Environmental Science* **2013,** *6* (8), 2265-2279, DOI: 10.1039/C3EE40871J.
(14) Ponrouch, A.; Frontera, C.; Bardé, F.; Palacín, M. R. Towards a Calcium-Based Rechargeable Battery. *Nature Materials* **2016,** *15* (2), 169-172, DOI: 10.1038/nmat4462.
(15) Wang, D.; Gao, X.; Chen, Y.; Jin, L.; Kuss, C.; Bruce, P. G. Plating and Stripping Calcium in an Organic Electrolyte. *Nature Materials* **2018,** *17* (1), 16-20, DOI: 10.1038/nmat5036.
(16) Tutusaus, O.; Mohtadi, R.; Arthur, T. S.; Mizuno, F.; Nelson, E. G.; Sevryugina, Y. V. An Efficient Halogen-Free Electrolyte for Use in Rechargeable Magnesium Batteries. *Angewandte Chemie International Edition* **2015,** *54* (27), 7900-7904, DOI: https://doi.org/10.1002/anie.201412202.
(17) Connell, J. G.; Genorio, B.; Lopes, P. P.; Strmcnik, D.; Stamenkovic, V. R.; Markovic, N. M. Tuning the Reversibility of Mg Anodes via Controlled Surface Passivation by H2O/Cl– in Organic Electrolytes. *Chemistry of Materials* **2016,** *28* (22), 8268-8277, DOI: 10.1021/acs.chemmater.6b03227.

(18) Esbenshade, J. L.; Barile, C. J.; Fister, T. T.; Bassett, K. L.; Fenter, P.; Nuzzo, R. G.; Gewirth, A. A. Improving Electrodeposition of Mg through an Open Circuit Potential Hold. *The Journal of Physical Chemistry C* **2015,** *119* (41), 23366-23372, DOI: 10.1021/acs.jpcc.5b07825.
(19) Sa, N.; Pan, B.; Saha-Shah, A.; Hubaud, A. A.; Vaughey, J. T.; Baker, L. A.; Liao, C.; Burrell, A. K. Role of Chloride for a Simple, Non-Grignard Mg Electrolyte in Ether-Based Solvents. *ACS Applied Materials & Interfaces* **2016,** *8* (25), 16002-16008, DOI: 10.1021/acsami.6b03193.
(20) Pan, B.; Huang, J.; He, M.; Brombosz, S. M.; Vaughey, J. T.; Zhang, L.; Burrell, A. K.; Zhang, Z.; Liao, C. The Role of MgCl2 as a Lewis Base in ROMgCl–MgCl2 Electrolytes for Magnesium-Ion Batteries. *ChemSusChem* **2016,** *9* (6), 595-599, DOI: https://doi.org/10.1002/cssc.201501557.
(21) Connell, J. G.; Zorko, M.; Agarwal, G.; Yang, M.; Liao, C.; Assary, R. S.; Strmcnik, D.; Markovic, N. M. Anion Association Strength as a Unifying Descriptor for the Reversibility of Divalent Metal Deposition in Nonaqueous Electrolytes. *ACS Applied Materials & Interfaces* **2020,** *12* (32), 36137-36147, DOI: 10.1021/acsami.0c09404.
(22) Chen, Y.; Jaegers, N. R.; Han, K. S.; Wang, H.; Young, R. P.; Agarwal, G.; Lipton, A. S.; Assary, R. S.; Washton, N. M.; Hu, J. Z.; Mueller, K. T.; Murugesan, V. Probing Conformational Evolution and Associated Dynamics of Mg(N(SO2CF3)2)2·Dimethoxyethane Adduct Using Solid-State 19F and 1H NMR. *The Journal of Physical Chemistry C* **2020,** *124* (9), 4999-5008, DOI: 10.1021/acs.jpcc.9b10212.
(23) Hahn, N. T.; Driscoll, D. M.; Yu, Z.; Sterbinsky, G. E.; Cheng, L.; Balasubramanian, M.; Zavadil, K. R. Influence of Ether Solvent and Anion Coordination on Electrochemical Behavior in Calcium Battery Electrolytes. *ACS Applied Energy Materials* **2020,** *3* (9), 8437-8447, DOI: 10.1021/acsaem.0c01070.
(24) Borodin, O.; Smith, G. D. LiTFSI Structure and Transport in Ethylene Carbonate from Molecular Dynamics Simulations. *The Journal of Physical Chemistry B* **2006,** *110* (10), 4971-4977, DOI: 10.1021/jp056249q.
(25) Li, T.; Balbuena, P. B. Theoretical Studies of Lithium Perchlorate in Ethylene Carbonate, Propylene Carbonate, and Their Mixtures. *Journal of The Electrochemical Society* **1999,** *146* (10), 3613-3622, DOI: 10.1149/1.1392523.
(26) Ong, M. T.; Verners, O.; Draeger, E. W.; van Duin, A. C. T.; Lordi, V.; Pask, J. E. Lithium Ion Solvation and Diffusion in Bulk Organic Electrolytes from First-Principles and Classical Reactive Molecular Dynamics. *The Journal of Physical Chemistry B* **2015,** *119* (4), 1535-1545, DOI: 10.1021/jp508184f.
(27) Han, S. Structure and Dynamics in the Lithium Solvation Shell of Nonaqueous Electrolytes. *Scientific Reports* **2019,** *9* (1), 5555, DOI: 10.1038/s41598-019-42050-y.
(28) Agarwal, G.; Doan, H. A.; Assary, R. S. Molecular Structure and Electron Affinity of Metal-Solvent Complexes: Insights from Density Functional Theory Simulations. *Journal of The Electrochemical Society* **2020,** *167* (10), 100545, DOI: 10.1149/1945-7111/ab9c7b.
(29) Baskin, A.; Prendergast, D. Ion Solvation Engineering: How to Manipulate the Multiplicity of the Coordination Environment of Multivalent Ions. *The Journal of Physical Chemistry Letters* **2020,** *11* (21), 9336-9343, DOI: 10.1021/acs.jpclett.0c02682.
(30) Camacho-Forero, L. E.; Smith, T. W.; Bertolini, S.; Balbuena, P. B. Reactivity at the Lithium–Metal Anode Surface of Lithium–Sulfur Batteries. *The Journal of Physical Chemistry C* **2015,** *119* (48), 26828-26839, DOI: 10.1021/acs.jpcc.5b08254.

(31) Camacho-Forero, L. E.; Smith, T. W.; Balbuena, P. B. Effects of High and Low Salt Concentration in Electrolytes at Lithium–Metal Anode Surfaces. *The Journal of Physical Chemistry C* **2017,** *121* (1), 182-194, DOI: 10.1021/acs.jpcc.6b10774.
(32) Camacho-Forero, L. E.; Balbuena, P. B. Elucidating Electrolyte Decomposition under Electron-Rich Environments at the Lithium-Metal Anode. *Physical Chemistry Chemical Physics* **2017,** *19* (45), 30861-30873, DOI: 10.1039/C7CP06485C.
(33) Camacho-Forero, L. E.; Balbuena, P. B. Effects of Charged Interfaces on Electrolyte Decomposition at the Lithium Metal Anode. *Journal of Power Sources* **2020,** *472*, 228449, DOI: https://doi.org/10.1016/j.jpowsour.2020.228449.
(34) Kamphaus, E. P.; Angarita-Gomez, S.; Qin, X.; Shao, M.; Engelhard, M.; Mueller, K. T.; Murugesan, V.; Balbuena, P. B. Role of Inorganic Surface Layer on Solid Electrolyte Interphase Evolution at Li-Metal Anodes. *ACS Applied Materials & Interfaces* **2019**, DOI: 10.1021/acsami.9b07587.
(35) Young, J.; Smeu, M. Ethylene Carbonate-Based Electrolyte Decomposition and Solid–Electrolyte Interphase Formation on Ca Metal Anodes. *The Journal of Physical Chemistry Letters* **2018,** *9* (12), 3295-3300, DOI: 10.1021/acs.jpclett.8b01261.
(36) Young, J.; Kulick, P. M.; Juran, T. R.; Smeu, M. Comparative Study of Ethylene Carbonate-Based Electrolyte Decomposition at Li, Ca, and Al Anode Interfaces. *ACS Applied Energy Materials* **2019,** *2* (3), 1676-1684, DOI: 10.1021/acsaem.8b01707.
(37) Das, S.; Bhauriyal, P.; Pathak, B. Theoretical Insights into Solid Electrolyte Interphase Formation in an Al Anode Dual-Ion Battery. *The Journal of Physical Chemistry C* **2020,** *124* (14), 7634-7643, DOI: 10.1021/acs.jpcc.9b11421.
(38) Lowe, J. S.; Siegel, D. J. Reaction Pathways for Solvent Decomposition on Magnesium Anodes. *The Journal of Physical Chemistry C* **2018,** *122* (20), 10714-10724, DOI: 10.1021/acs.jpcc.8b01752.
(39) Baskin, A.; Prendergast, D. Exploration of the Detailed Conditions for Reductive Stability of Mg(TFSI)2 in Diglyme: Implications for Multivalent Electrolytes. *The Journal of Physical Chemistry C* **2016,** *120* (7), 3583-3594, DOI: 10.1021/acs.jpcc.5b08999.
(40) Han, K. S.; Hahn, N. T.; Zavadil, K. R.; Jaegers, N. R.; Chen, Y.; Hu, J. Z.; Murugesan, V.; Mueller, K. T. Factors Influencing Preferential Anion Interactions during Solvation of Multivalent Cations in Ethereal Solvents. *The Journal of Physical Chemistry C* **2021**, DOI: 10.1021/acs.jpcc.0c09830.
(41) Rajput, N. N.; Qu, X.; Sa, N.; Burrell, A. K.; Persson, K. A. The Coupling between Stability and Ion Pair Formation in Magnesium Electrolytes from First-Principles Quantum Mechanics and Classical Molecular Dynamics. *Journal of the American Chemical Society* **2015,** *137* (9), 3411-3420, DOI: 10.1021/jacs.5b01004.
(42) Kresse, G.; Furthmüller, J. Efficiency of Ab-Initio Total Energy Calculations for Metals and Semiconductors using a Plane-Wave Basis Set. *Computational Materials Science* **1996,** *6* (1), 15-50, DOI: https://doi.org/10.1016/0927-0256(96)00008-0.
(43) Kresse, G.; Furthmüller, J. Efficient Iterative Schemes for Ab Initio Total-Energy Calculations using a Plane-Wave Basis Set. *Physical Review B* **1996,** *54* (16), 11169-11186, DOI: 10.1103/PhysRevB.54.11169.
(44) Kresse, G.; Hafner, J. Ab Initio Molecular Dynamics for Liquid Metals. *Physical Review B* **1993,** *47* (1), 558-561, DOI: 10.1103/PhysRevB.47.558.

(45) Kresse, G.; Hafner, J. Ab Initio Molecular-Dynamics Simulation of the Liquid-Metal--Amorphous-Semiconductor Transition in Germanium. *Physical Review B* **1994,** *49* (20), 14251-14269, DOI: 10.1103/PhysRevB.49.14251.
(46) Perdew, J. P.; Burke, K.; Ernzerhof, M. Generalized Gradient Approximation Made Simple. *Physical Review Letters* **1996,** *77* (18), 3865-3868, DOI: 10.1103/PhysRevLett.77.3865.
(47) Grimme, S.; Antony, J.; Ehrlich, S.; Krieg, H. A Consistent and Accurate Ab Initio Parametrization of Density Functional Dispersion Correction (DFT-D) for the 94 Elements H-Pu. *The Journal of Chemical Physics* **2010,** *132* (15), 154104, DOI: 10.1063/1.3382344.
(48) Blöchl, P. E. Projector Augmented-Wave Method. *Physical Review B* **1994,** *50* (24), 17953-17979, DOI: 10.1103/PhysRevB.50.17953.
(49) Hohenberg, P.; Kohn, W. Inhomogeneous Electron Gas. *Physical Review* **1964,** *136* (3B), B864-B871, DOI: 10.1103/PhysRev.136.B864.
(50) Kresse, G.; Joubert, D. From Ultrasoft Pseudopotentials to the Projector Augmented-Wave Method. *Physical Review B* **1999,** *59* (3), 1758-1775, DOI: 10.1103/PhysRevB.59.1758.
(51) Martínez, L.; Andrade, R.; Birgin, E. G.; Martínez, J. M. PACKMOL: A Package for Building Initial Configurations for Molecular Dynamics Simulations. *Journal of Computational Chemistry* **2009,** *30* (13), 2157-2164, DOI: https://doi.org/10.1002/jcc.21224.
(52) Shterenberg, I.; Salama, M.; Yoo, H. D.; Gofer, Y.; Park, J.-B.; Sun, Y.-K.; Aurbach, D. Evaluation of (CF3SO2) 2N−(TFSI) Based Electrolyte Solutions for Mg Batteries. *Journal of The Electrochemical Society* **2015,** *162* (13), A7118.
(53) Ha, S.-Y.; Lee, Y.-W.; Woo, S. W.; Koo, B.; Kim, J.-S.; Cho, J.; Lee, K. T.; Choi, N.-S. Magnesium(II) Bis(trifluoromethane sulfonyl) Imide-Based Electrolytes with Wide Electrochemical Windows for Rechargeable Magnesium Batteries. *ACS Applied Materials & Interfaces* **2014,** *6* (6), 4063-4073, DOI: 10.1021/am405619v.
(54) Frisch, M. J.; Trucks, G. W.; Schlegel, H. B.; Scuseria, G. E.; Robb, M. A.; Cheeseman, J. R.; Scalmani, G.; Barone, V.; Petersson, G. A.; Nakatsuji, H.; Li, X.; Caricato, M.; Marenich, A. V.; Bloino, J.; Janesko, B. G.; Gomperts, R.; Mennucci, B.; Hratchian, H. P.; Ortiz, J. V.; Izmaylov, A. F.; Sonnenberg, J. L.; Williams; Ding, F.; Lipparini, F.; Egidi, F.; Goings, J.; Peng, B.; Petrone, A.; Henderson, T.; Ranasinghe, D.; Zakrzewski, V. G.; Gao, J.; Rega, N.; Zheng, G.; Liang, W.; Hada, M.; Ehara, M.; Toyota, K.; Fukuda, R.; Hasegawa, J.; Ishida, M.; Nakajima, T.; Honda, Y.; Kitao, O.; Nakai, H.; Vreven, T.; Throssell, K.; Montgomery Jr., J. A.; Peralta, J. E.; Ogliaro, F.; Bearpark, M. J.; Heyd, J. J.; Brothers, E. N.; Kudin, K. N.; Staroverov, V. N.; Keith, T. A.; Kobayashi, R.; Normand, J.; Raghavachari, K.; Rendell, A. P.; Burant, J. C.; Iyengar, S. S.; Tomasi, J.; Cossi, M.; Millam, J. M.; Klene, M.; Adamo, C.; Cammi, R.; Ochterski, J. W.; Martin, R. L.; Morokuma, K.; Farkas, O.; Foresman, J. B.; Fox, D. J. *Gaussian 16 Rev. C.01*, Wallingford, CT, 2016.
(55) Chai, J.-D.; Head-Gordon, M. Long-Range Corrected Hybrid Density Functionals with Damped Atom–Atom Dispersion Corrections. *Physical Chemistry Chemical Physics* **2008,** *10* (44), 6615-6620, DOI: 10.1039/B810189B.
(56) Baskin, A.; Lawson, J. W.; Prendergast, D. Anion-Assisted Delivery of Multivalent Cations to Inert Electrodes. *The Journal of Physical Chemistry Letters* **2021,** *12* (18), 4347-4356, DOI: 10.1021/acs.jpclett.1c00943.
(57) Bader, R. F. W. Atoms in Molecules. *Accounts of Chemical Research* **1985,** *18* (1), 9-15, DOI: 10.1021/ar00109a003.

(58) Henkelman, G.; Arnaldsson, A.; Jónsson, H. A Fast and Robust Algorithm for Bader Decomposition of Charge Density. *Computational Materials Science* **2006,** *36* (3), 354-360, DOI: https://doi.org/10.1016/j.commatsci.2005.04.010.
(59) Sanville, E.; Kenny, S. D.; Smith, R.; Henkelman, G. Improved Grid-Based Algorithm for Bader Charge Allocation. *Journal of Computational Chemistry* **2007,** *28* (5), 899-908, DOI: 10.1002/jcc.20575.
(60) Tang, W.; Sanville, E.; Henkelman, G. A Grid-Based Bader Analysis Algorithm without Lattice Bias. *Journal of Physics: Condensed Matter* **2009,** *21* (8), 084204, DOI: 10.1088/0953-8984/21/8/084204.

Table of contents Graphic

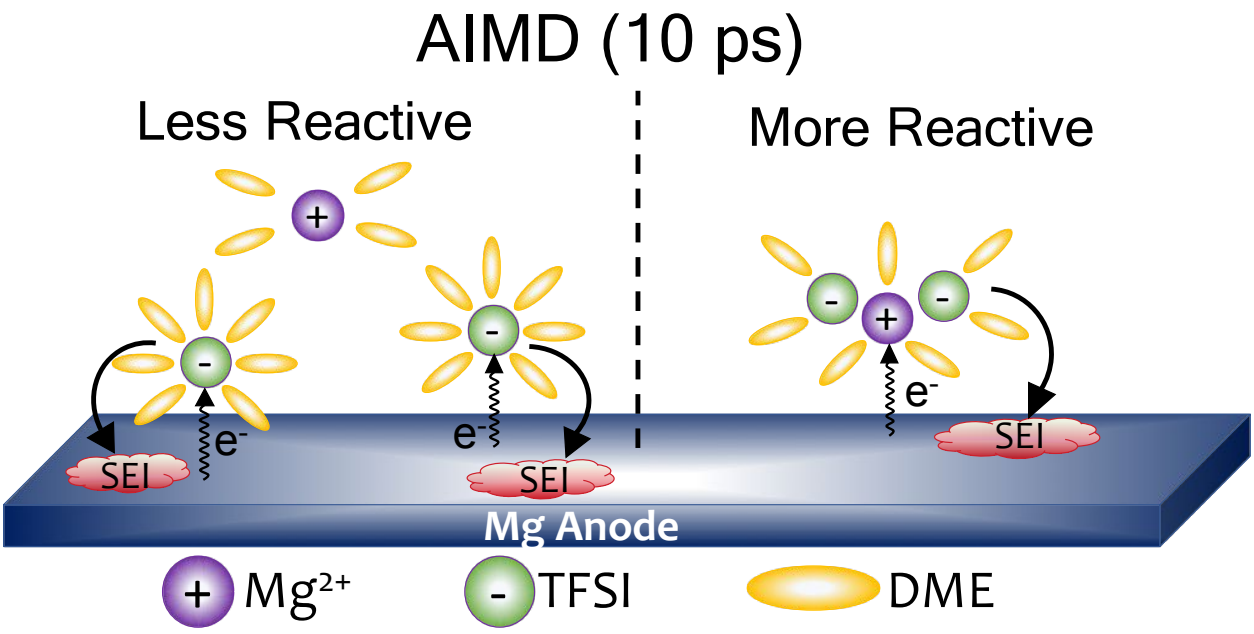
AIMD (10 ps)
Less Reactive
More Reactive
+
-
e-
SEI
Mg Anode
Mg2+
TFSI
DME

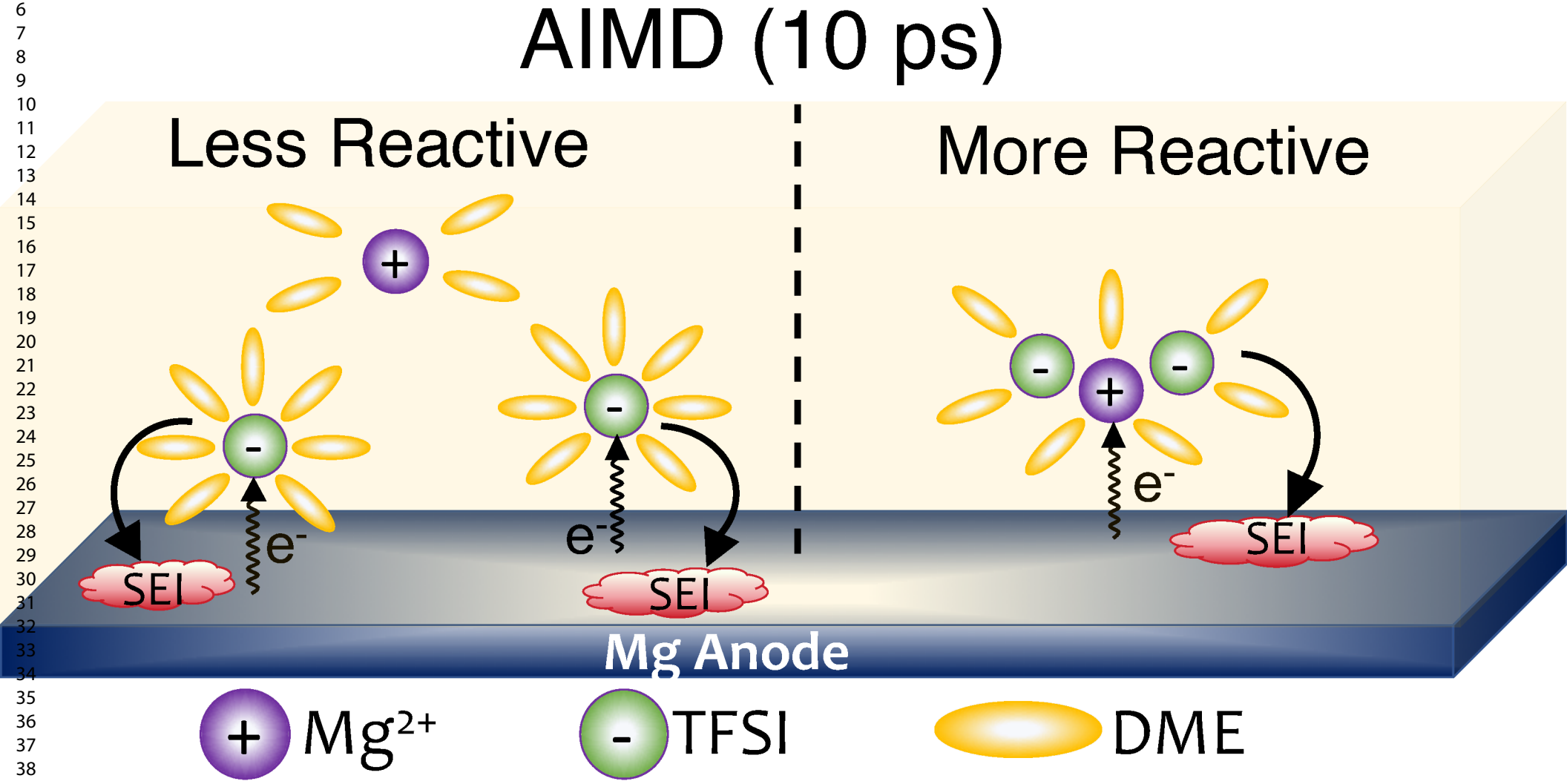
AIMD (10 ps)
Less Reactive
More Reactive
+
-
e-
SEI
Mg Anode
Mg2+
TFSI
DME